## 3.3.2 Properties of site-selective Pd aerosol activation and Cu micropatterining onto FPI

Figure 51(a) shows the size distribution of spark generated aerosol nanoparticles measured using the SMPS system. The geometric mean diameter and geometric standard deviation were 108.7 nm and 1.5, respectively. The total number concentration was 6.9 x 10^6 particles/cm^3. The morphology and structure of the particles were characterized by a HRTEM and a XPS, respectively. The HRTEM micrograph (Figure 51(b)) reveals that the particles were agglomerates of several primary particles (each ~28 Å in diameter). Figure 51(b) also shows the SAED pattern corresponding to the HRTEM micrograph. The pattern had diffraction lines showing [111] and [200] reflections and a weak diffraction line showing [220] of the face-centered cubic (fcc) lattice for metallic palladium. The XPS profile (Figure 51(c)) of the particles reveals that they were pure palladium. The binding energy (BE) doublet with the BEs for the Pd $3d_{5/2}$ and Pd $3d_{3/2}$ peak components located at about 335 and 340 eV, respectively, are assigned to the Pd^0 species [Persson et al., 2007]. Figure 51(d) shows FESEM images of the particles in line and square patterns. The FESEM images show that the particles are spread out over the entire line and square. The FESEM images also show that the thermophoretic focusing of the particles (see Figure 52(a)) resulted in a line (24 μm in width) and a square (136 μm width x 136 μm length), which are much narrower than those of the mask holes.
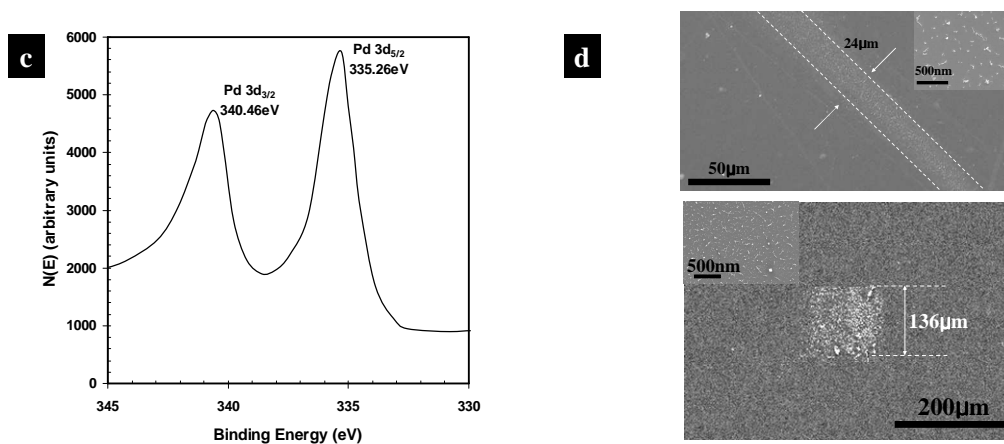

99
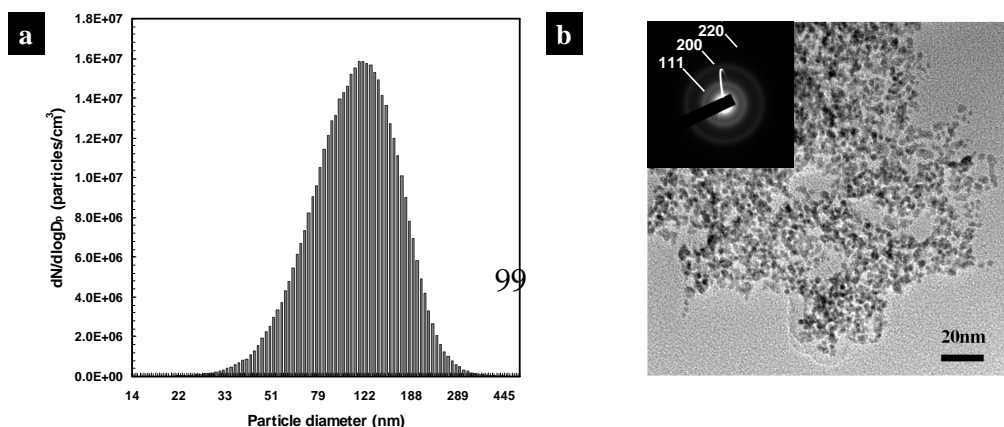
Figure 51. Particle characterization of catalytic aerosol activation. (a) Particle size distribution of spark generated aerosol nanoparticles. (b) HRTEM image and a SAED pattern (inset) of spark generated particles. (c) XPS profile of spark generated particles. (d) FESEM images of line and square patterns in PI substrate.

To understand the effect of thermophoresis on particle deposition, velocities and temperatures of the particle-laden flow were calculated using a commercial CFD code (Fluent

6.3) with a finite volume grid containing approximately 5,000 cells. Thermophoretic particle

motion is usually described by the thermophoretic particle velocity:

$$v_{th} = -K_{th} \frac{\mu_g \nabla T}{\rho_g T_p} \tag{5}$$

where ∇T represents the temperature gradient in the vicinity of the particle. μ_g is the gas

dynamic viscosity, T_p the particle temperature, ρ_g the gas density. K_{th} is the

thermophoretic coefficient, which increases with decreasing of the particle size. As shown in

Figure 52(a), the particles were expected to be selectively deposited on the PI substrate by

thermophoresis due to the temperature distribution inside the dotted area A. Figure 4b shows

the distribution of thermophoretic y-direction velocities, as a function of particle size, inside

the dotted area A in Figure 52(b). The thermophoretic velocities for all the particles were

higher than the average velocity of the particle-laden flow toward the mask.
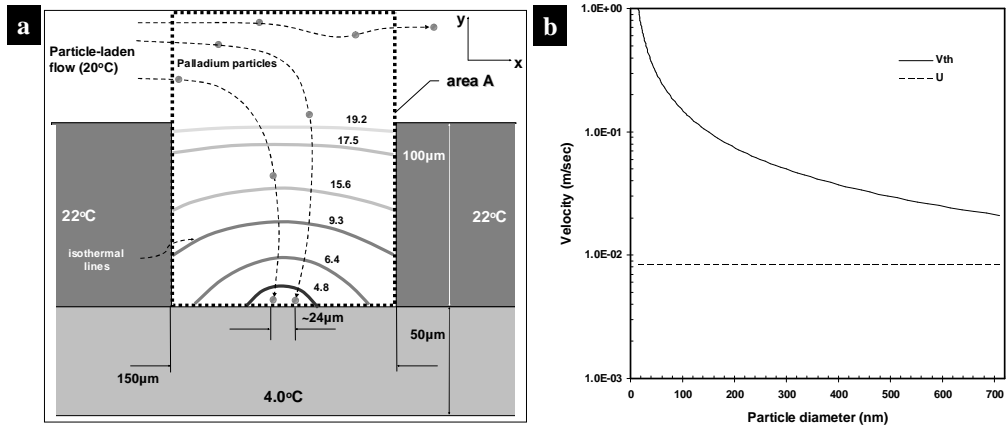
Figure 52. (a) Temperature distribution inside the area A of Figure 38. (b) Thermophoretic velocity distribution as a function of particle size. U is the average upstream velocity of the particle-laden flow.

As shown in Figure 53(a), the copper ELD occurred only on the palladium nanoparticles, i.e., at the activated sites of the PI substrate. The palladium nanoparticles effectively acted as a seed to initiate the copper ELD. The copper patterns were wider than those of palladium patterns (24 μm in width for line, 136 μm x 136 μm for square, as shown in Figure 51(d)) because ELD is an isotropic process. The optical microscopy analysis revealed that patterns having 35 μm in width for a line and 165 μm x 165 μm for a square were obtained from the ELD (Figure 53(a)). FESEM pictures corresponding to Figure 53(a) show that copper particles were densely packed (Figure 53(b)). From the EDX analysis (also shown in Figure 53(b)) it was found that the coated metal consisted mainly of copper, but contained a small amount of palladium as well as carbon and oxygen, which may have originated from the PI substrate. The XRD profile of the copper pattern shows that there exist three peaks located at $2\theta=43.3$, 50.4, and 74.1^{o} (Figure 53(c)). Compared with the data from the powder diffraction file No. 04-0836, these peaks correspond to the [111], [200], and [220] planes of the fcc phase for copper. The XRD profile shows the characteristics of pure metallic copper with a good crystallinity and without any impurity phase. The average particle size evaluated according to Scherrer's formula was approximately 46 nm. An AFM was used to determine the dimensions of the copper patterns. Figure 53(d) shows the 2D AFM profile obtained from Figure 53(d). The height and root mean squared roughness were about 1.6 μm and 56 nm, respectively.
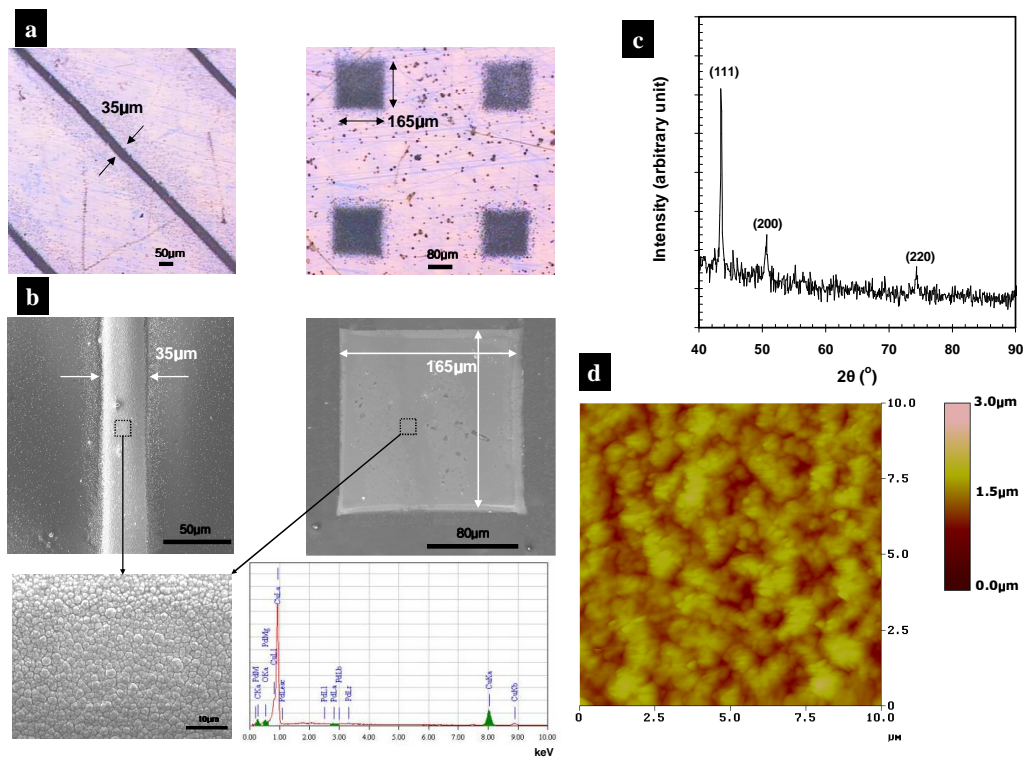
Figure 53. Results of copper ELD. (a) Optical microscopy images of the copper patterns (left:
slanting lines, right: square arrays). (b) FESEM micrographs corresponding to the optical

microscopy images with a high-magnitude FESEM image and an EDX profile. (c) XRD profile. (d) 2D AFM profile.

Resistivities (ρ) of the copper line pattern were calculated through the relationship $\rho = RA/L$, where R, A, L are the resistance, cross-sectional area, and length of the pattern, respectively. The average value of the resistivities was approximately 4.6 $\mu\Omega \cdot$cm, which is almost comparable to the theoretical resistivity of bulk copper (1.7 $\mu\Omega \cdot$cm).

Other copper patterns using different pattern masks were also demonstrated (Figure 54). Two stainless steel pattern masks having an angled-line array (150 μm in width) and a circled-line array (50 μm in width) were used to obtain copper patterns having the dimensions of 32 μm in width and 8 μm in width, respectively.

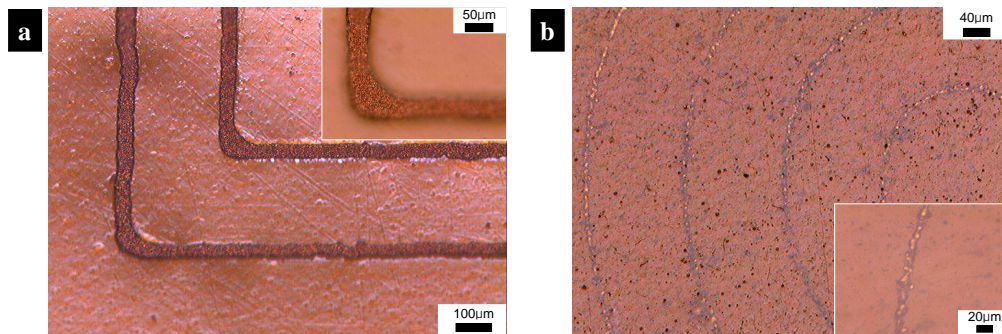Figure 54. Other copper micropatterns using different pattern masks. (a) Optical microscopy image for an angled-line array (32 μm in width). (b) Optical microscopy image for a fine circled-line (8 μm in width).

Using our site-selective aerosol activation and ELD processes, it was possible to create stable and selective copper patterns with micrometer dimensions on a flexible PI substrate. Our processes were simple and environmentally benign, and can be applied in order to produce display electronics circuits, sensors, radio-frequency identification (RFID) transponders, and other microelectronic devices.

3.3.3 Properties of site-selective Pt aerosol activation and Ag micropatterining onto FPI

The size distribution of the platinum nanoparticles was measured using a SMPS and is provided in Figure 55(c). The electrical mobility diameter of the particles ranged from 20 to 200 nm. The morphology and structure of the particles were characterized by a HRTEM-SAED pattern and XPS. For the characterizations, the airborne particles were directly sampled on a porous carbon-coated copper grid. The HRTEM micrograph (inset of Figure 55(c)) reveals that the platinum particles were agglomerates of several primary particles (each ~26Å in diameter). Figure 55(d) shows the SAED pattern corresponding to the HRTEM micrograph. The pattern has sharp diffraction lines showing [111] and [200] reflections and weak diffraction lines showing [220] and [311] of the fcc lattice for metallic platinum. In addition, Figure 55(e) shows the XPS profile for the particles revealing that the particles were pure platinum. The BE doublet with the BEs for the Pt $4f_{7/2}$ and Pt $4f_{5/2}$ peak components lying at about 71.1 and 74.4 eV, respectively, are assigned to the Pt^0 species [Tian et al., 2006].
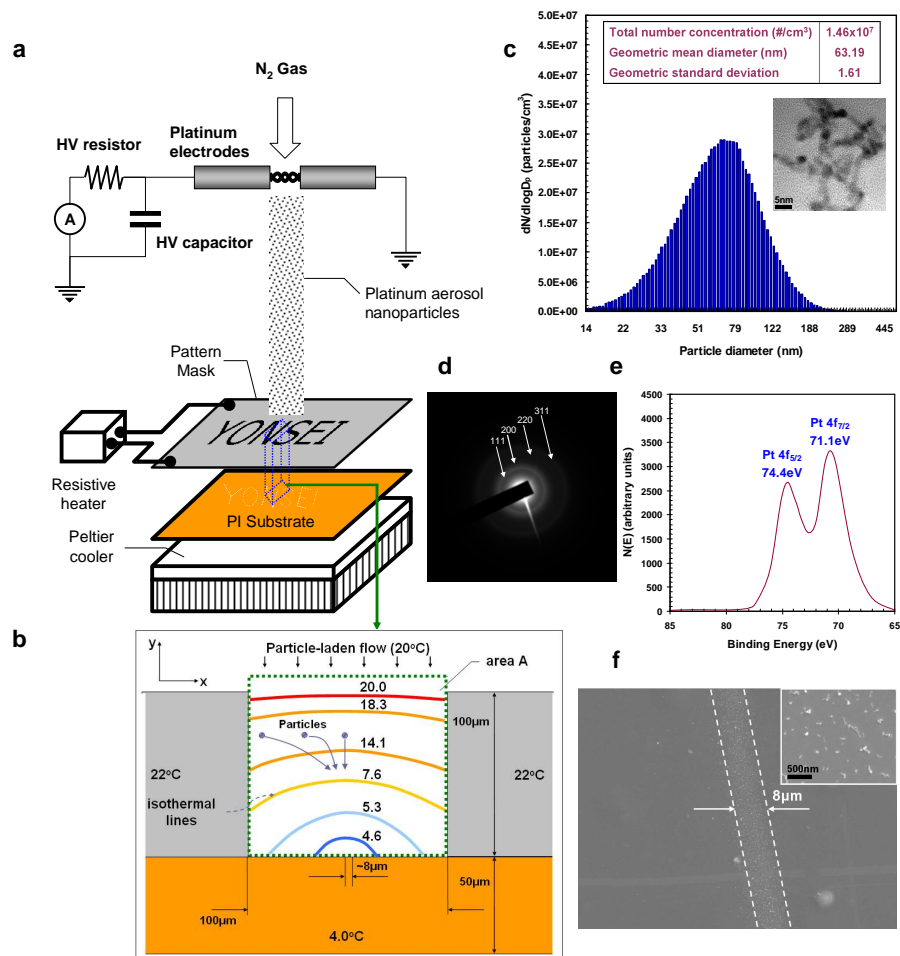
Figure 55. Overview of surface activation and particle charcterization. (a) Surface activation by spark generated nanoparticles. Platinum aerosol nanoparticles were generated by a spark generator while a resistively heated YONSEI pattern mask was placed on a PI substrate cooled by a Peltier cooler. The particles were delivered to the surface of the PI substrate through the YONSEI pattern hole. (b) A temperature distribution inside the area A. (c) A particle size distribution with a HRTEM image (inset) of spark generated platinum particles. (d) A SAED pattern of the particles. (e) A XPS profile of the particles. (f) A FESEM image of YONSEI in the PI substrate.

106

The PI substrate was then separated from the mask and annealed at 190°C for 5 minutes in air to prevent detachment of the particles from the PI substrate. Figure 55(f) shows a FESEM image of the particles in a line of the "YONSEI" pattern. The FESEM image shows that the particles are spread out over the entire line.

The FESEM image also shows that the thermophoretic focusing of the particles (see Figure 55(b)) resulted in a line width of ~8μm, which is much narrower than the width of the hole (100 μm) in the mask. The thermophoretic velocities (Supplementary Data 4) for all the particles were higher than the average velocity of the particle-laden flow toward the mask. The velocities and temperatures of the particle-laden flow were calculated using a CFD code (Fluent 6.3) with a finite volume grid containing approximately 44,000 cells.

The PI substrate was immersed in a silver ELD solution at 20°C for the deposition of silver on the platinum nanoparticles. Figure 56(a) shows that a silver overlayer of "YONSEI" onto the activated PI substrate was subsequently formed during the process. The overall reactions are described in the inset of Figure 56(a). The PI substrate was rinsed with deionized water after it was removed from the ELD solution to remove the residual and then set aside to dry. Figure 56(b) shows a photo of the "YONSEI" silver pattern. The optical microscopy analysis of Figure 56(b) revealed that line patterns having a width of 18μm were obtained (Figure 56(c)). As shown in Figure 56(c), the silver ELD occurred only on the platinum nanoparticles, i.e., at the activated region of the PI substrate. The platinum nanoparticles effectively acted as a seed to initiate the silver ELD. The line width of silver patterns (18 μm) was wider than that of platinum patterns (~8 μm, as shown in Figure 55(f)) because ELD is an isotropic process. A FESEM picture of a silver line pattern shows that silver particles were densely packed (Figure 56(d)). From the EDX analysis (Figure 56(e)) it was found that the coated metal consitsted mainly of silver, but contained a small amount of platinum as well as

107

carbon and oxygen, which may have originated from the PI substrate. The XRD profile of the silver pattern shows that there exist five peaks located at $2\theta=38.2$, 44.4, 64.5, 77.5, and 81.6° (Figure 56(f)). Compared with the data from the powder diffraction file No. 04-0783, these peaks correspond to the [111], [200], [220], [311], and [222] planes of the fcc phase for silver. The XRD profile shows the characteristics of pure metallic silver with a good crystallinity and without any impurity phase. The average particle size evaluated according to Scherrer's formula was approximately 35nm.

AFM was used to determine the dimensions of the silver pattern. Figure 57 shows the 2 and 3D AFM profiles obtained from Figure 56(c). The height and root mean squared roughness were about 1μm and 50nm, respectively.

Resistivities (ρ) of the "YONSEI" silver pattern were calculated through the relationship $\rho = RA/L$, where R, A, L are the resistance, cross-sectional area, and length of the pattern, respectively. The average value of the resistivities was approximately 6.8 μΩ·cm, which is almost comparable to the theoretical resistivity of bulk silver (1.6 μΩ·cm).

Figure 56. Results of silver ELD. (a) A scheme of silver ELD onto the YONSEI platinum pattern. (b) A YONSEI silver pattern. (c) Optical microscopy images of YONSEI silver pattern. (d) A FESEM micrograph corresponding to the optical microscopy images. (e) An EDX profile. (f) A XRD profile.
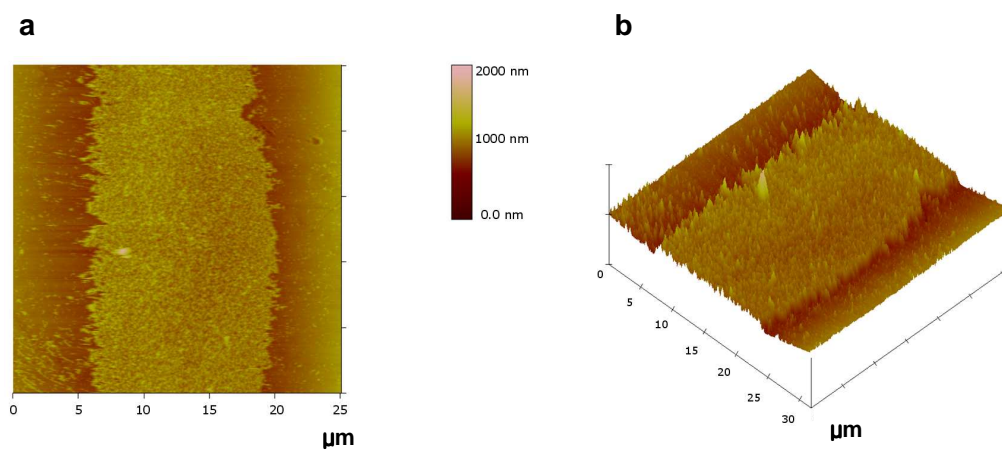
109

Figure 57. Topographs of YONSEI silver pattern. (a) A 2D image. (b) A 3D image.

3.4 Summaries and conclusions

Using aerosol activation and ELD, it was possible to create stable silver layers on ACF. When the deposition time was 10 minutes and the activation intensity increased from 0.23 to 4.25 mg/g (palladium/ACF), aerosol activation increased the silver deposition from 7.1 to 13.2 mg/g (silver/ACF), increased the average size of silver particles from 4.9 to 38.8 nm, decreased the surface area of ACF from 1382 to 1286 m^2/g, and decreased the pore volume of ACF from 0.77 to 0.67 cm^3/g.

A site-selective catalytic activation by producing palladium aerosol nanoparticles via spark generation and then thermophoretically depositing the particles onto a flexible polyimide substrate through the pattern holes of a mask was introduced. After thermal curing, the activated substrate is placed into a solution for electroless copper deposition; the copper patterns of a line (35 μm in width) and a square (165 μm x 165 μm) were reproducibly formed. Both patterns had the height of 1.6 μm. The average value of the resistivities for the copper line patterns was approximately 4.6 μΩ·cm, which is almost comparable to the theoretical resistivity of bulk copper (1.7 μΩ·cm). Furthermore, the angled-line array (32 μm in width) and circled-line array (8 μm in width) copper micropatterns using different pattern masks were also achieved.

Using platinum aerosol nanoparticles and a silver ELD solution, silver line patterns having a width of 18 μm and a height of 1μm were created with the ability to be effectively reproduced. The average value of the resistivities was approximately 6.8 μΩ·cm, which is almost comparable to the theoretical resistivity of bulk silver (1.6 μΩ·cm).

Supplementary Data 1

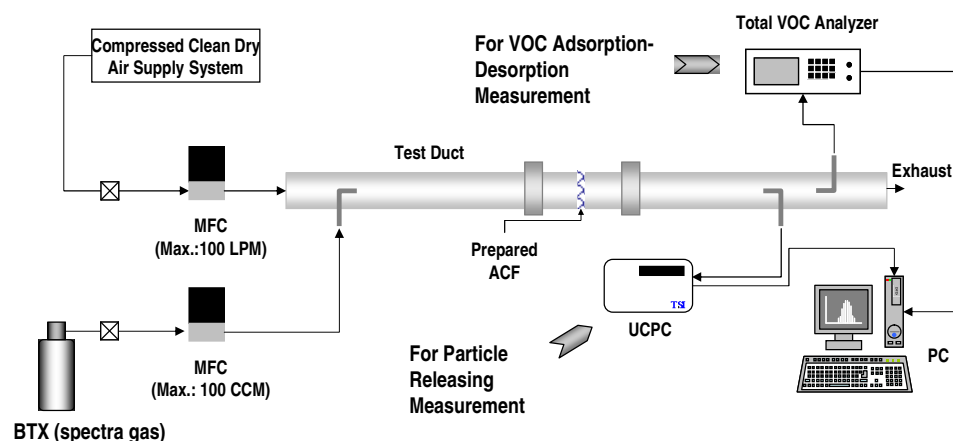## S1. 1. Experimental setup for VOC adsorption-desorption

Figure 1S. Experimental set-up for VOC adsorption-desorption.

ACF have a larger micropore volume and a more uniform micropore size distribution than GAC, and thus, they are considered to have a larger adsorption capacity and greater rates of adsorption [Li et al., 1998; Shen et al., 2006; Fu & Dai, 2004; Park et al., 2004; Mochida et al., 2000; Vilaplana-Ortego et al., 2002] than GAC. ACF have recently been considered to be a promising adsorbent for controlling VOC. However, most of the studies conducted on the adsorption of VOC by ACF have pertained to equilibrium conditions, with the primary objective being the development of an appropriate isotherm. Only a few studies on the adsorption of VOC by ACF have been conducted for dynamic conditions [Das et al., 2004].

The experimental setup shown in Figure 1S consisted of BTX apparatus (Spectra Gases, model VOC) and carrier gas supply section, test duct section, and VOC detection section. The cylindrical test duct made of duralumin had a volume of 1,963 cm^3 (5 cm (D)×100 cm (L)).

The duct temperature was maintained at 296 K ± 1 K. The face velocity was 0.5 m/sec, which belonged to a practical range of 0.25-0.50 m/sec [Tsai et al., 2000]. Stainless steel (SS) sampling ports and Teflon tubings were used to connect the duct with the analytical instruments. Every prepared ACF sample was initially dried under vacuum at 393 K overnight and then it was fixed on a filter holder in the test duct. Two SS meshes were used at both ends of each sample (50 mm in diameter and 2 mm in depth) to support the sample. Acquired from a compressed gas cylinder, the BTX gases with a mixing ratio of 0.47:0.45:0.09 were used as the reactant gas at a concentration of 981.6 ppmv, using air as the balance gas according to National Institute of Standards and Technology (NIST) standards. Clean compressed air from a dry clean air supply system carried the BTX gas stream to the test duct. The flow rates of the BTX gas stream and the clean air stream were 0.1-100 mL/min and 0.1-100 L/min respectively, and they were controlled by two mass flow controllers (Tylan, US). BTX gas in air at room temperature was delivered to the test duct and then it was mixed with clean air resulting in a BTX concentration of 1ppmv at the inlet of the duct.

S1. 2. Stability of copper particles coated on ACF

Before investigating the effect of copper deposition time on the adsorption and desorption of VOC, the prepared samples' resistance to air flow was checked by measuring the amount of copper aerosol particles detached from each sample by using an ultrafine condensation particle counter (UCPC, TSI 3025A). The sample was exposed to injected particle-free air at a face velocity of 0.5 m/sec. Figure 2S shows that the concentration of aerosol particles varied with time for all samples. The sample deposited with Cu-30 released the highest amount of particles; however, the concentration became negligible after 100

seconds. After the stability of copper particles deposited on the ACF samples was checked, experiments on the adsorption and desorption of VOC were conducted.
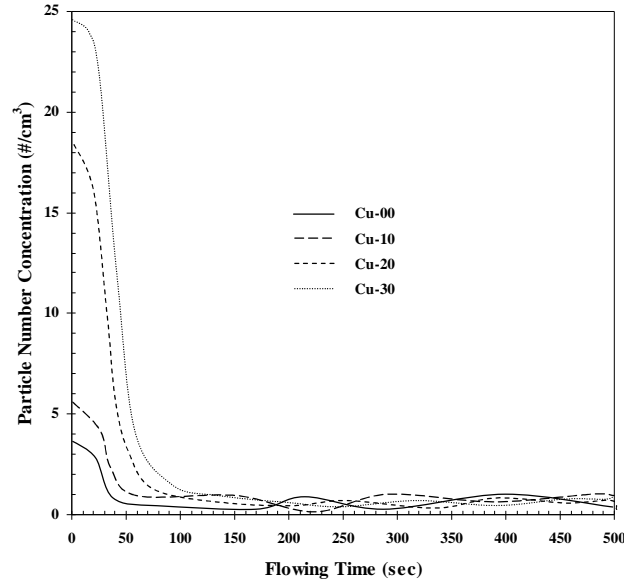

Figure 2S. Particle detachment characteristics during air flow (@ 0.5 m/s of air velocity).

S1. 3. Amounts and effective diffusivities of adsorbed and desorbed VOC

The amounts of adsorbed and desorbed VOC by the ACF samples were calculated by using the following equation:

$$m \, (mg \, of \, VOC \, / \, g \, of \, ACF) \; = \; m_f^{-1} \int_0^t f \, (C_i - C_e) \, Q dt \qquad (1S)$$

where m is the ratio between the mass of the adsorbed VOC (or the desorbed VOC) and the mass of the pristine ACF sample (m_f), t (min) is the VOC adsorption time (or VOC desorption

time when the BTX gas supply is stopped), f is the unit conversion factor (ppm to mg/m^3), C_i is the influent VOC concentration (ppmv), C_e is the effluent concentration (ppmv), and Q is the air flow rate (L/min).

The combined diffusivity inside the pores was defined as the harmonic average of Knudsen and molecular diffusivities [Bird et al., 1960; Das et al., 2004; Smith, 1996; Yang et al., 1997] and is given by

$$\frac{1}{D} = \frac{1}{D_k} + \frac{1}{D_m} \tag{2S}$$

where, D_m is the molecular diffusivity. The Knudsen diffusivity is given by

$$D_k = \frac{2 \times r_p}{3} \left(\frac{8RT}{\pi M} \right)^{\frac{1}{2}} \approx 97 \times R_{pore} \left(\frac{T}{M} \right)^{\frac{1}{2}} \tag{3S}$$

where, R_{pore} = pore radius in m, M = molecular weight in g/mol, T = temperature in K, D_k = Knudsen diffusivity in cm^2/sec.

Finally, the effective diffusivity inside the pores is determined by using the formula

$$D_e = \frac{\alpha D}{\tau} \tag{4S}$$

where, α = intrafiber void fraction, τ = tortuosity factor.
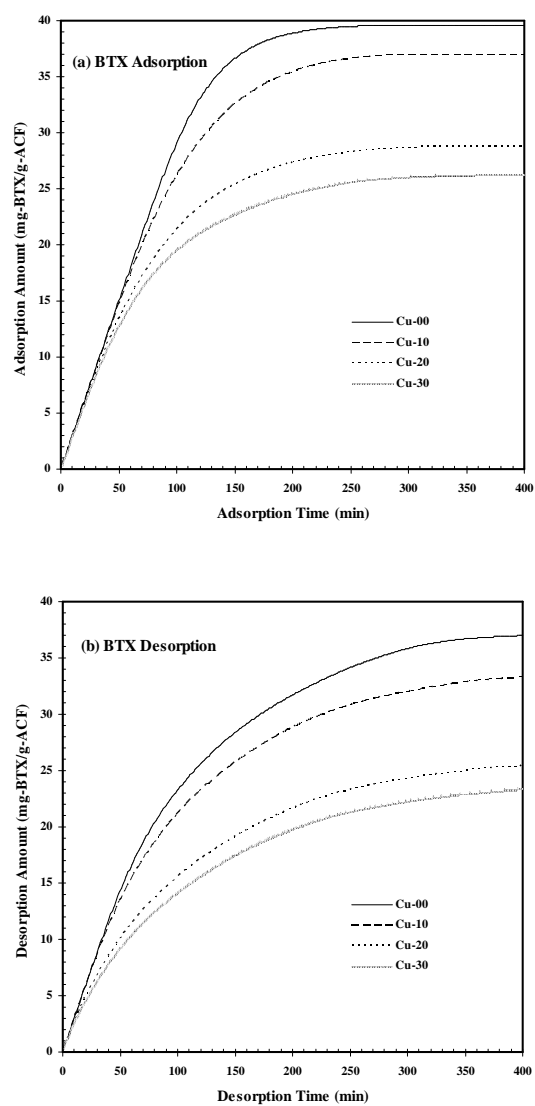
Figure 3S. VOC adsorption and desorption amounts of the pristine and the copper deposited
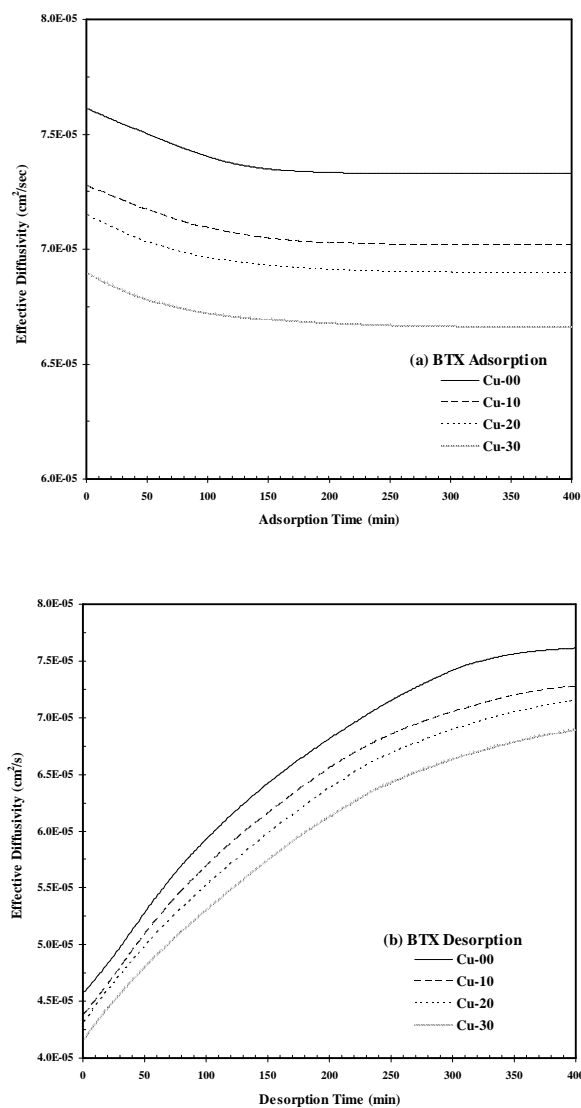ACF.

Figure 4S. Effective diffusivities of VOC adsorption and desorption of the pristine and the copper deposited ACF.

Figures 3S and 4S show the amounts and effective diffusivities of VOC adsorption and desorption that were calculated by using equation (1S) and equations (2S)-(4S), respectively.

The amounts of Cu-00 after 400 minutes were 40 mg-BTX/g-ACF and 35 mg-BTX/g-ACF for adsorption and desorption tests, respectively. Moreover, the ranges of effective diffusivity for Cu-00 during 400 minutes were approximately $7.3\text{-}7.7 \times 10^{-5}$ cm^2/sec and $4.6\text{-}7.6 \times 10^{-5}$ cm^2/sec for adsorption and desorption tests, respectively. These amounts and effective diffusivities were higher than those of the other samples due to the higher specific surface area (or pore volume).
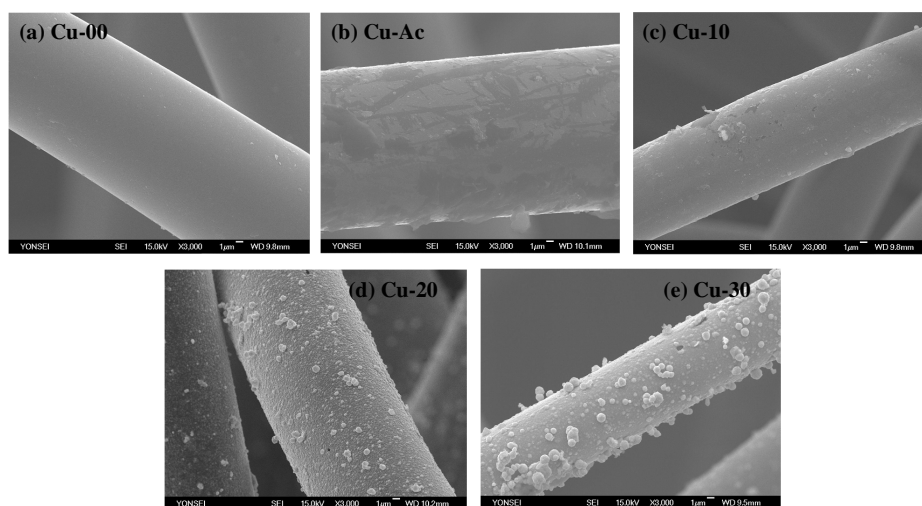
S1. 4. SEM results

Figure 5S. SEM micrographs of the pristine, catalytically activated and the copper deposited ACF.

Figure 5S shows the FESEM micrographs of the prepared ACF samples. Cu-10, Cu-20, and Cu-30 represent the copper deposited ACF at deposition times of 10, 20, and 30 minutes, respectively, while Cu-00 and Cu-Ac represent the pristine ACF and the catalytically activated ACF, respectively. As the deposition time increased, there were more particles on the surface

of the fiber and the particles grew larger. Particles having a "snowflake" shape or aggregates of 50 nm-1 μm are displayed in Figure 5(c)-5(e).

S1. 5. EDX results

Chemical analysis was performed via EDX (JED-2300, JEOL, Japan). The EDX results of Figure 6S show that any sample contained carbon, copper, and a small amount of oxygen. The observed oxygen may have originated from the commercially purchased ACF for this study. Figure 6S shows that while Cu-00 had no copper peak, the copper-deposited ACF samples had some peaks of CuKa, CuLa, etc., which indicated the presence of copper on the ACF samples. Cu-Ac contained a minute amount of tin, which might have been originated from the Pd-Sn activation process. Even though palladium was not detected in the EDX results, from the ICP-AES analyse, the concentration of palladium particles was found to be about 350 ppm, which was below the EDX detection limit (refer to Main text).

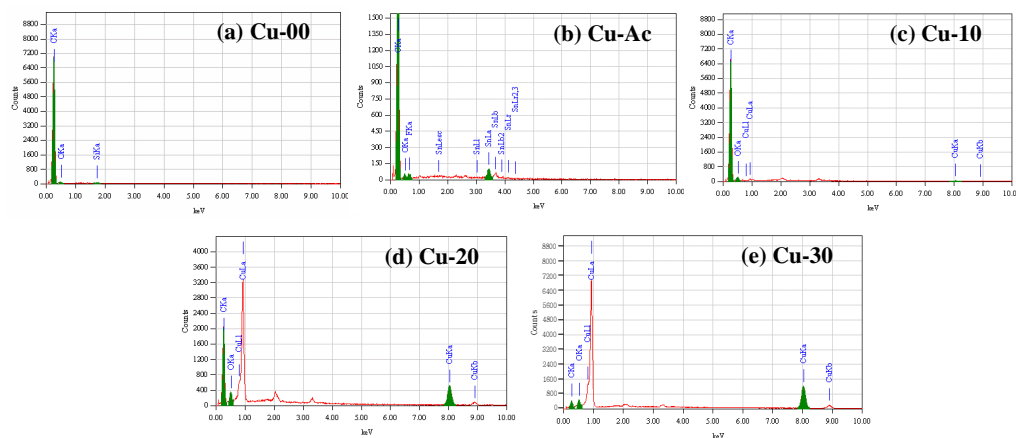Figure 6S. EDX profiles of the pristine, catalytically activated and the copper-deposited ACF.

119

S1.6. BET results

To understand the effect of excessive amount of copper on VOC adsorption and desorption, the textural properties of the copper deposited ACF were measured. Figure 7S shows that the major uptake occurred at a relatively low pressure ($P/P_o<0.1$) and reached a plateau at $P/P_o \approx 0.3$. The data implies that all of the ACF samples had microporous characteristics (type I isotherm) according to the IUPAC classification [Brunauer et al., 1938]. The adsorption amount was the highest for Cu-00. However, it decreased as the amount of copper increased. Figure 8S shows that the pore size distributions of all the samples were concentrated for pore diameters smaller than 30 Å. The pores within porous materials are typically classified as either micropores (<20 Å), mesopores (20-500 Å), or macropores (>500 Å), in accordance with IUPAC classification [Brunauer et al., 1938]. Figure 8S shows a fairly homogeneous microporous size distribution. The decrease of pore volumes with an increase in the amount of copper is due to copper particles obstructing the pore wall. Detailed results on the textural properties of the samples are summarized in Table 1S. The TSSA, MSSA, APD, TPV and MPV decreased with increasing deposition time. The adsorption characteristics observed on the copper deposited ACF samples are indicative of reduced adsorption due to the possible loss of active sites for adsorption. Therefore, the amount of copper must be controlled for the determination of optimal VOC adsorption. From these results, it was concluded that both the fluid-to-fiber mass transfer resistance and/or intraparticle (pore) resistance controlled the adsorption (or desorption) of VOC on the ACF, and all the dynamics were solely determined by the adsorption (or desorption) rates.

120
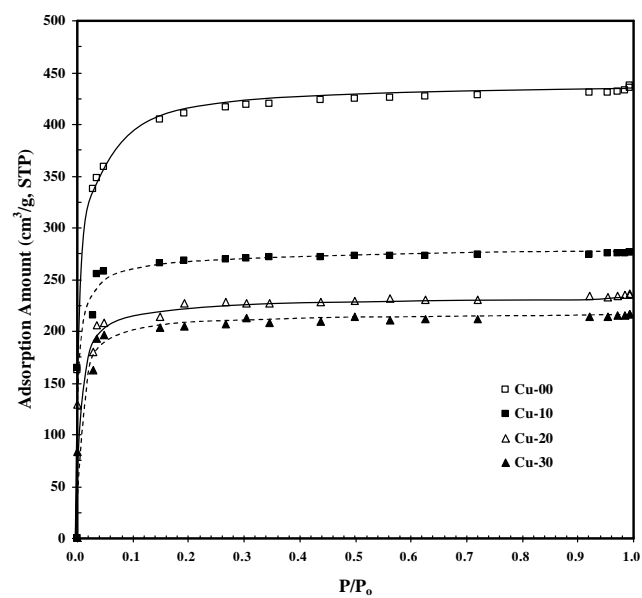
Figure 7S. Adsorption isotherms of N_2 at 77.4 K of the pristine and the copper deposited ACF.

121

Figure 8S. Pore size distributions of the pristine and the copper deposited ACF.

Table 1S Textural properties of copper-deposited ACF

	TSSA (m^2/g)	MSSA (m^2/g)	TPV (cm^3/g)	MPV (cm^3/g)	APD (Å)
Cu-00	1,598	1583	0.91	0.86	17.7
Cu-10	931	929	0.69	0.65	16.9
Cu-20	865	860	0.59	0.55	16.6
Cu-30	814	808	0.53	0.50	16.0

Supplementary Data 2

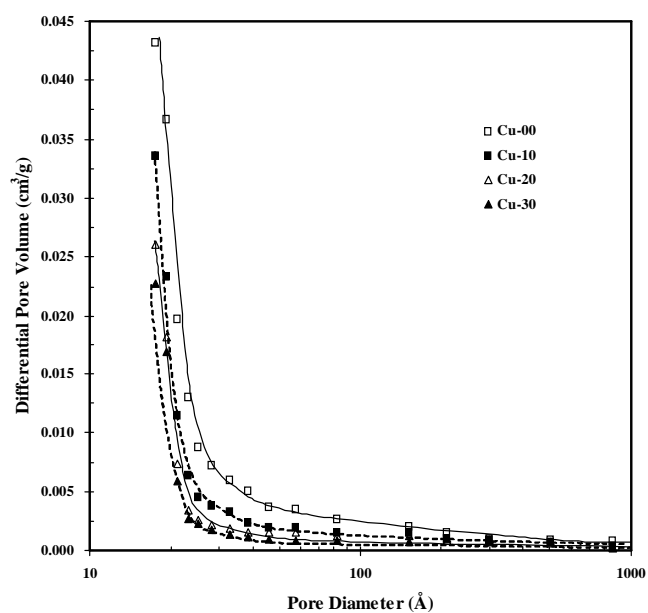## S2. 1. ELD of Ag on thin-MWNT

The TEM images (Figure 9S) show that silver particles (10-80 nm) much larger than those in the Main Text (~1.5 nm) were deposited only on the exterior surfaces of the thin-MWNTs (6-9 nm in diameter and 10-20 μm in length, respectively; CMP-340F, Iljin Nanotech, Korea), even though the inner diameters of the thin-MWNTs were as large as those used by Ugarte et al. (1996 & 1998) (4 nm) for silver filling. This difference might be due to the different reaction conditions (e-beam decomposition of silver nitrate vs electroless deposition of silver) and/or mass transfer inhibition by the formerly deposited silver particles near the open end of the thin-MWNTs, as shown in Figure 9S(d). The formation of silver particles much larger than those in the Main Text might be due to the high number of catalytically activated sites. For thin-MWNTs, unlike the MWNTs in the Main Text, the activated sites would exist only on the exterior surfaces, so rapid nucleation and the subsequent deposition of silver on the exterior surfaces could be achieved.
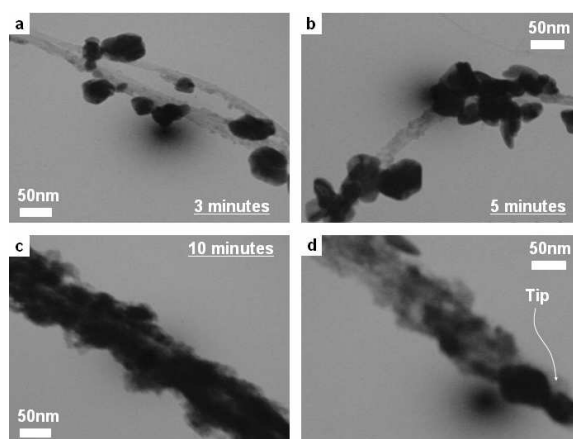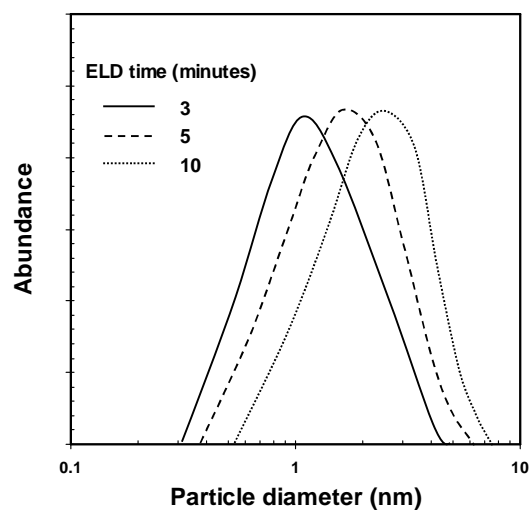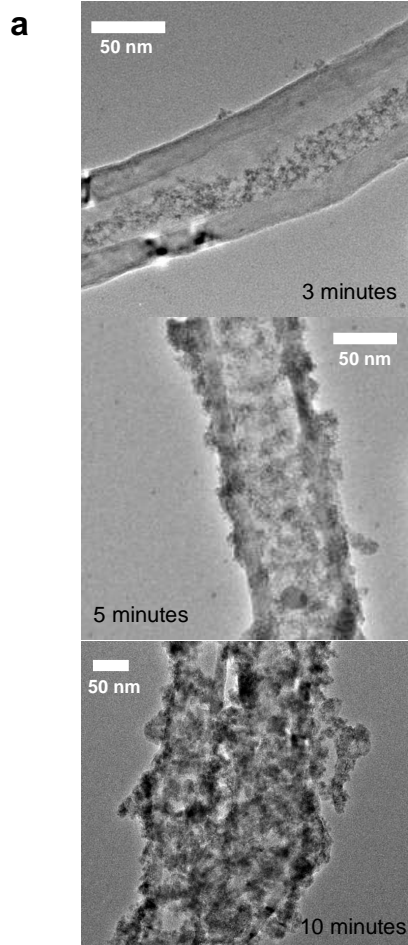

Figure 9S. TEM micrographs of the silver deposited thin-MWNTs for (a) 3, (b) 5, and (c) 10 minutes. (d) TEM image near the open end of thin-MWNTs (for 5 minutes of ELD).
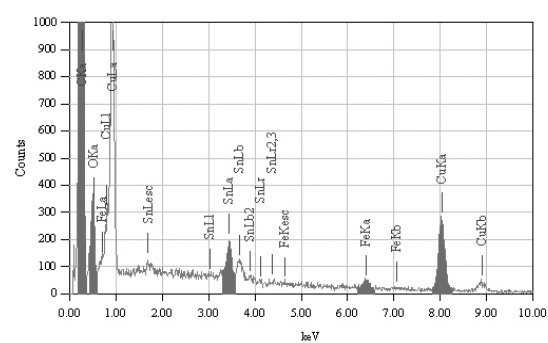
S2. 2. ELD of Cu on the MWNT

After carrying out the pre-treatment processes reported in the Main Text, the MWNTs were immersed into a solution for the ELD of copper. The copper ELD solution was a mixture of solutions A and B at a 10:1 (v/v) ratio. Solution A contained 3 g of $CuSO_4$, 14 g of sodium potassium tartrate (Rochelle salt), and 4 g of NaOH in 100 mL of deionized water. Solution B was an aqueous formaldehyde solution (37.2 wt%). The pre-treated MWNTs were immersed into the mixture for 3-10 minutes at 20^oC to allow copper particles to deposit on the MWNTs. Figure 10S(a) shows HRTEM images of copper MWNTs when the copper deposition time increased from 3 to 10 minutes. The copper nanoparticles were deposited selectively onto the interior surfaces of the MWNTs. When the ELD time was 5 minutes, copper particles were deposited on both the interior and exterior surfaces of the MWNTs. The copper deposition layer further grew when the ELD time was prolonged to 10 minutes. Figure 10S(a) also shows copper particle size distribution and EDX profile. The mean diameter of the copper particles was 1.1, 1.7, and 2.3 nm for 3, 5, and 10 minutes of ELD time, respectively. The EDX profile showed peaks for copper, along with peaks for carbon, oxygen, iron, and tin. The copper-to-carbon fraction was increased from 6.66 to 25.51% in mass (0.90 to 4.60% in atom) when the ELD time was increased from 3 to 10 minutes. Although there were some minor differences, such as the metal-to-carbon fraction and average crystallite size between silver and copper ELD, the progress of metallization on the MWNTs were similar for both silver and copper.

Figure 10S(b) gives the XRD profiles showing the major diffraction peaks for copper particles. The peaks at 43.2, 50.3, and 74.1^o (2θ) were assigned to the [111], [200], and [220] planes of the fcc phase of copper. The average crystal sizes of the copper particles calculated using the Scherrer formula were 0.7, 1.9, and 1.4 nm for an ELD time of 3, 5, and 10 minutes, respectively.

a

50 nm

3 minutes

50 nm

5 minutes

50 nm

10 minutes

[EDX profile]

b

c
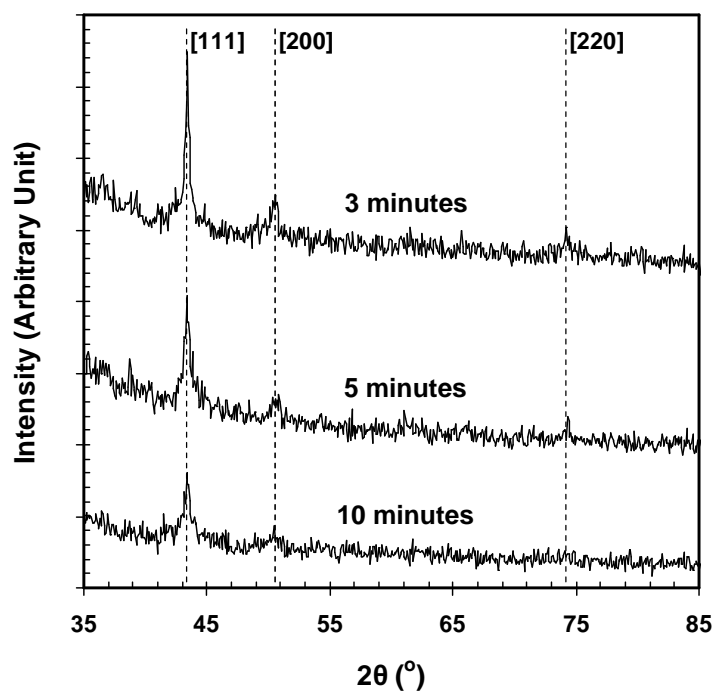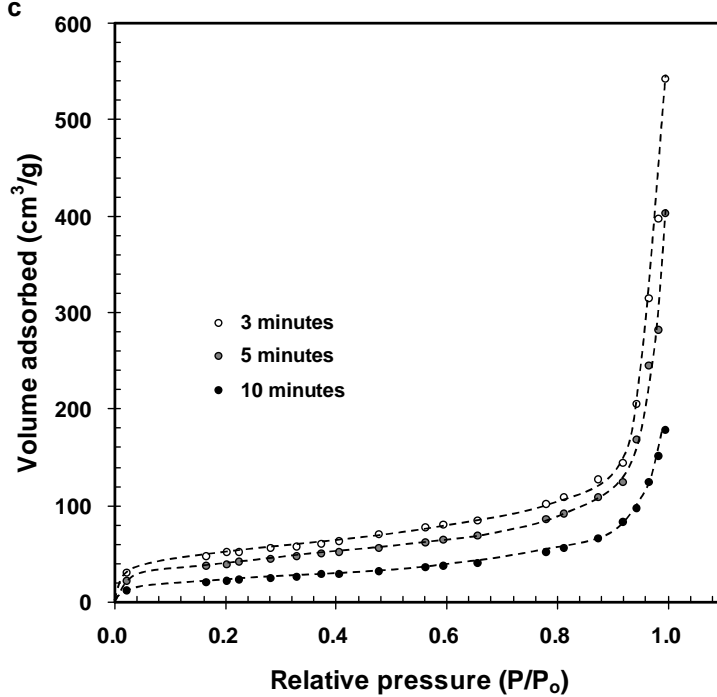
Items	Total		Microporous		Mesoporous		APD ^{c} (Å)
Samples	SA ^{a} (m^2/g)	PV ^{b} (cm^3/g)	SA (m^2/g)	PV (cm^3/g)	SA (m^2/g)	PV (cm^3/g)	
3 minutes	202.79	0.771	32.62	0.067	170.17	0.704	177.43
5 minutes	146.67	0.622	24.07	0.026	122.60	0.596	171.90
10 minutes	81.22	0.268	8.81	0.018	72.41	0.250	138.29

^{a} "SA" is the surface area, ^{b} "PV" is the pore volume, and ^{c} "APD" is the average pore diameter.

Figure 10S. Characterization of copper coated MWNTs. (a) Morphological and chemical analyses. (b) XRD profiles. (c) Adsorption isotherms and textural properties.

Figure 10S(c) shows the nitrogen adsorption isotherms of the copper deposited MWNTs at 77 K. All sampled exhibited a type II isotherm according to the IUPAC classification. The amount of nitrogen adsorbed was inversely proportional to the ELD time. The surface areas and volumes of the micro and mesopores, and the mean pore diameters are also shown in Figure 10S(c).

Supplementary Data 3

S3. 1. Particle size distributions of spark generated particles

The size distribution (Figure 11S) of the spark generated aerosol particles was measured using a scanning mobility particle sizer (SMPS) system, which consisted of an electrostatic classifier (TSI 3081), a condensation particle counter (TSI 3025), and an aerosol charge neutralizer. The SMPS system was operated with a sample flow of 0.3 L/min, a sheath flow of 3 L/min, and a scan time of 180 seconds (measurement range of between 13.8 and 723 nm). The electrical mobility equivalent diameter of all the particles ranged from 30 and 600 nm, and the geometric mean diameter, geometric standard deviation, and total number concentration for the graphite-graphite (denoted as Graphite), nickel-graphite, cobalt-graphite, and iron-graphite sparks are also described in Figure 11S. The size distribution of the graphite-graphite and metal-graphite sparks was similar even though the mechanism for their formation was different.

	Graphite	Ni-Graphite	Co-Graphite	Fe-Graphite
Geometric Mean Diameter (nm)	119.00	142.00	150.00	125.00
Geometric Standard Deviation	1.72	1.57	1.58	1.60
Total Concentration (particles/cm^3)	1.64E+07	1.47E+07	1.56E+07	1.31E+07
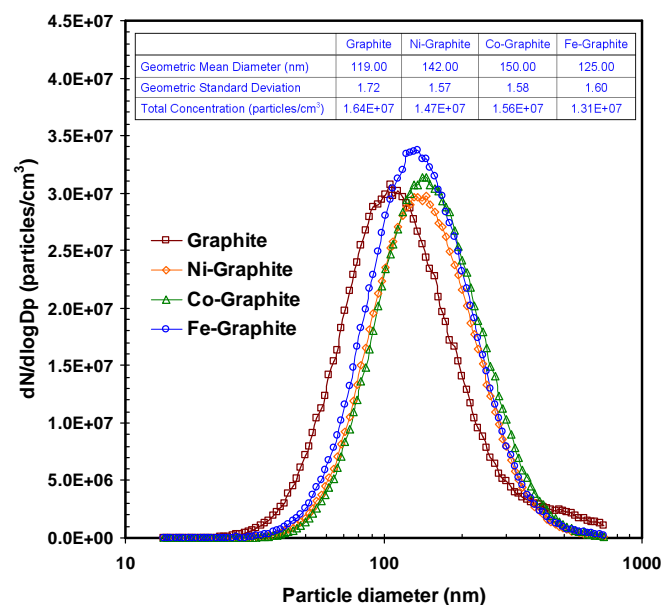
Figure 11S. Size distributions of the spark generated particles

S3. 2. Spark generated particles (anode: Co, cathode: C) and their characterizations

Figure 12S. Spark generated particles (anode: Co, cathode: C) and their characterizations. (a) TEM image and local EDX information (inset) of the spark generated particles. (b) TEM image of the CEMN and their size distribution (inset). (c) High magnitude TEM image of the CEMN. (d) Number of graphitic shells and the Co-to-C mass fraction vs CEMN (or Co core) diameter. (e) XRD pattern and Raman (inset) spectrum of the spark generated particles.

Figure 12S(a) shows a TEM image of the spark generated particles, which is similar to the nickel-graphite spark generation case, as described in the Main Text. The inset in Figure 12S(a) also shows local EDX information revealing the presence of Co and C. The

129

morphology (Figures 12S(b)-12S(c)) of the CEMN in the high magnitude TEM images is also similar to the nickel-graphite case. One possible reason for this similarity might be due to their similar activation energy [Host et al., 1997; Hwang et al., 1997; Saito, 1995; Saito et al., 1993a & 1994] for carbon diffusion into a metal. However, the CEMNs in the particle sample ranged in diameter from 12 to 448 nm (geometric mean diameter of 120 nm), which is larger than the nickel-graphite case. This might be due to higher metal-to-carbon mass fraction (0.28) than observed in the nickel-graphite case (0.23). The number of graphitic shells and the Co-to-C mass fraction vs the CEMN (or Co core) diameter were 3-28 and 0.26-0.89, respectively, as shown in Figure 12S(d). XRD (Figure 12S(e)) indicates that cores of the particles in Figure 12S(a) are in the form of element Co. The Raman peaks (inset of Figure 1S2(e)) at 1571 and 1339 cm^{-1} demonstrate the particle sample to have an I_G:I_D ratio of 1.06. The larger values of the graphitic shells and larger I_G:I_D ratio than those in the nickel-graphite case may also correspond to the Co-to-C mass fraction.

S3. 4. CEMNs and carbon nanotubes from the iron-graphite spark and their characterizations
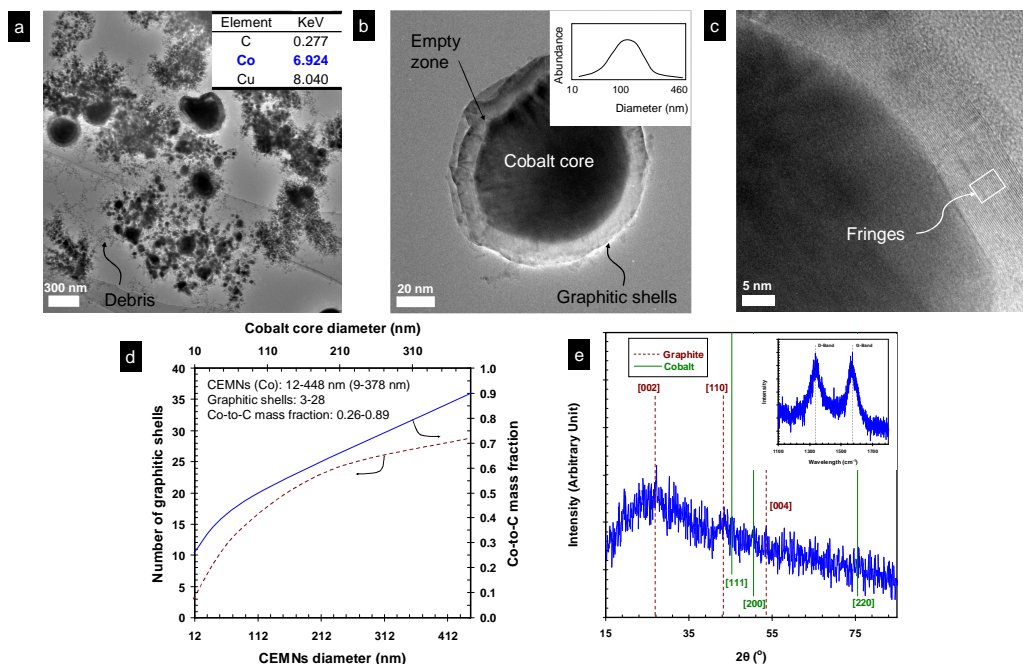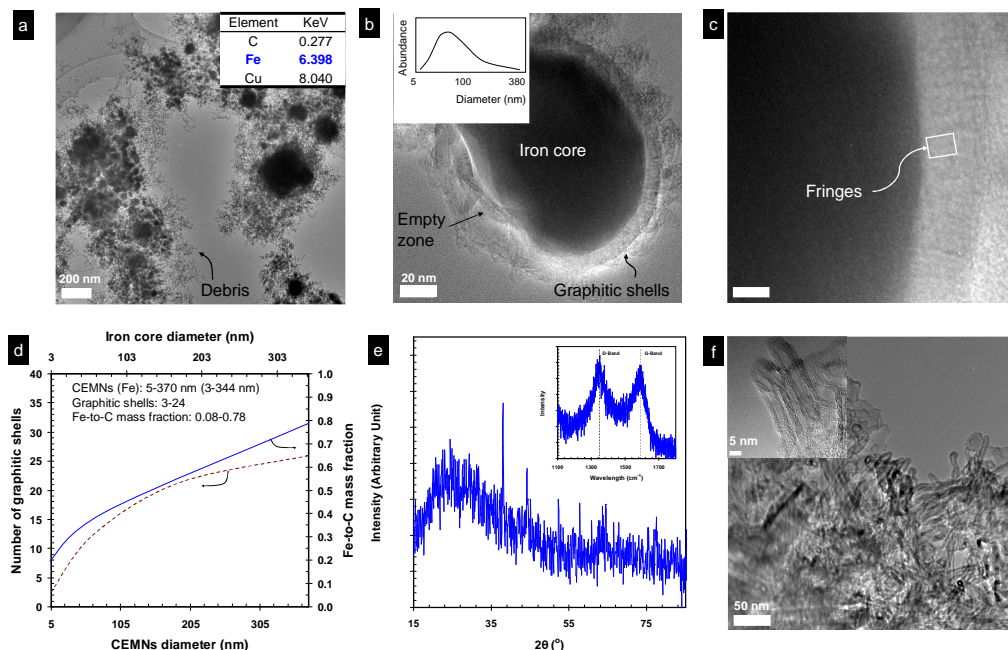

Figure 13S. Spark generated particles (anode: Fe, cathode: C) and their characterization. (a) TEM image and local EDX information (inset) of the spark generated particles. (b) TEM image of CEMN and the size distribution (inset) of CEMN. (c) High magnitude TEM image of the CEMN. (d) Number of graphitic shells and the Fe-to-C mass fraction vs CEMN (or Fe core) diameter. (e) XRD and Raman (inset) spectra of the spark generated particles. (f) TEM images of the spark-generated multiwall carbon nanotubes.

Figure 13S(a) shows a TEM image of the spark generated particles, which is similar to the nickel-graphite case in the Main Text or the cobalt-graphite case in Figure 12S. An inset of Fig. 13S(a) also shows local EDX information, revealing the presence of Fe and C. The

morphology (Figure 13S(b)-13S(c)) of the CEMN in the high magnitude TEM images is also similar to the nickel-graphite and cobalt-graphite cases. However, the CEMNs in the particle sample ranged in diameter from 5 to 370 nm (geometric mean diameter = 72 nm), which is smaller than the nickel-graphite or cobalt-graphite cases. One possible reason for this difference may be the lower metal-to-carbon mass fraction (0.11) than that in the nickel-graphite (0.23) or cobalt-graphite cases (0.22). Fig. 13S(d) shows that the number of graphitic shells and the Fe-to-C mass fraction as a function of the CEMN (or Fe core) diameter are 3-24 and 0.08-0.78, respectively. The smaller number of graphitic shells than that in the nickel-graphite case or the cobalt-graphite case may also correspond to the Fe-to-C mass fraction. The XRD profile (Figure 13S(e)) shows the presence of peaks associated with Fe_3C and α-Fe phases. The Fe_3C phases, with diffraction peaks at 37.6^o, 40.8^o, 42.8^o, 43.6^o, 44.1^o, 44.9^o, 45.7^o, 49.1^o, 54.3^o, 58.2^o, 78.4^o, and 86.0^o appear in the particle sample. The other peaks appearing at $2\theta = 44.67^o$, 65.02^o, and 82.33^o were assigned to the [110], [200], and [211] reflections of α-Fe, respectively. Based on the order of activation energies for carbon diffusion into a metal: Fe-C (10.5-16.5 kcal/more) < Co-C (34.7 kcal/mol) ~ Ni-C (33.0-34.8kcal/mol) [Rodriguez, 1993; Wang et al., 2003; Wang et al., 2007], it may be concluded that carbide particles are formed more easily from elemental Fe than from Ni or Co [Rodriguez, 1993]. The Raman peaks (inset of Figure 13S(e)) at 1592 and 1347 cm^{-1} demonstrate the spark generated particle sample to have an I_G:I_D ratio of 0.93, which is remarkably high even though its metal-to-carbon fraction is smaller than that in the cobalt-graphite case. Numerous carbon nanotubes (Figure 13S(f)) were occasionally observed in the spark generated particle sample and have a mean internal and external diameter of 3.5 nm and 9.2 nm, respectively. This corresponds to the activation energy for carbon nanotube growth: Fe-C (16.1 kcal/mol) < Co-C (33.0-33.3 kcal/mol) ~ Ni-C

(34.7 kcal/mol) [Rodriguez, 1993]. Therefore, the lowest activation energy of Fe-C might be one reason for nanotubes being observed only in the iron-graphite case.

S3. 5. Yields of CEMNs as a function of mass fraction of metal-to-carbon

The elemental composition of the spark generated particles was analyzed by EDX, and the results and corresponding yields of CEMN are shown in Table 2S. The yield was determined by the area fraction of CEMNs-to-all particles in the TEM image. In order to understand the effect of the metal-to-carbon mass fraction, the fraction was controlled by switching the electrode polarity of the spark. For metal (anode)-graphite (cathode) sparks, the metal-to-carbon mass fractions for Co and Fe were 0.28 and 0.11, respectively, with a CEMN yield of 0.61 (Co) and 0.53 (Fe). For the metal (cathode)-graphite (anode) sparks, the metal-to-carbon mass fractions were 0.09 and 0.04 for Co and Fe, respectively, with a CEMN yield of 0.30 (Co) and 0.18 (Fe). These results correspond to previous studies [Ang et al., 2004; Elliott et al., 1997; Flahaut et al., 2002; Host et al., 1997 & 1998a; Hwang et al., 1997; Jiao & Seraphin, 2000; Lu et al., 2005; Setlur et al., 1998; Teng et al., 2007], which used a modified arc system to generate a high metal-to-carbon mass fraction, leading to significant improvement in CEMN production. A previous study [Teng et al., 2007] reported that the encapsulation of all metal particles during CEMN production required only a slightly higher fraction of carbon than metal.

Table 2S Yields of CEMN as a function of the metal-to-carbon mass fraction

Sample	Metal to carbon fraction		Yield of CEMNs	
	Metal (anode) -Graphite (cathode)	Metal (cathode) -Graphite (anode)	Metal (anode) -Graphite (cathode)	Metal (cathode) -Graphite (anode)
Cobalt-graphite	0.28	0.09	0.61	0.30
Iron-graphite	0.11	0.04	0.53	0.18

Supplementary Data 4

S4. 1. Details for thermophoretic effect

Figure 14S shows the distribution of thermophoretic y-direction velocities, as a function of particle size, inside the dotted area A in Figure 55(a) in the Main Text.
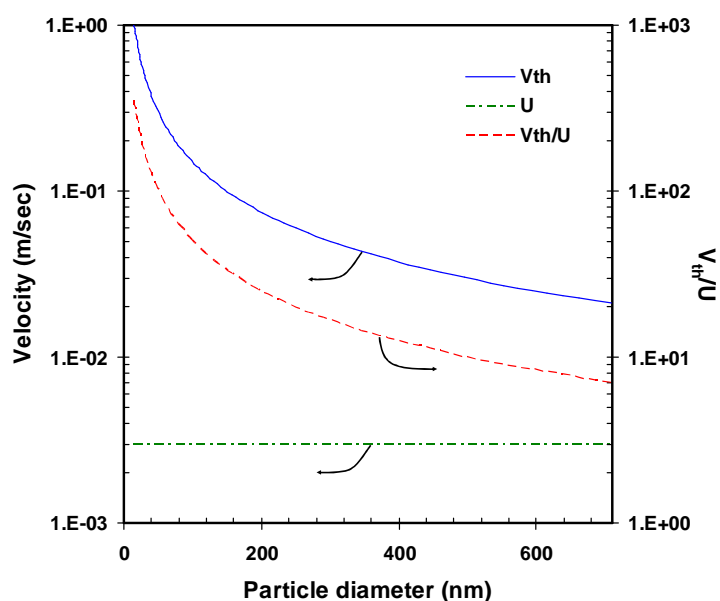
Figure 14S. Thermophoretic velocity distribution as a function of particle size. U is the average upstream velocity of the particle-laden flow.

S4. 2. Other silver patterns using different pattern masks

Silver square arrays were successfully formed on a PI substrate as shown in Figure 15S(a). A ultrafine silver line pattern of about 4 μm in width on a PI substrate was achieved as shown in Figure 15S(a). Dimensions of two stainless steel pattern masks for Figures 15S(a) and 15S(b) were 150 (width) x 150 (length) μm^2 and 50 (in width) μm, respectively.

Figure 15S. Other silver patterns using different pattern masks. (a) An optical microscopy image for silver square arrays (65×65 μm^2). (b) An optical microscopy image for a ultrafine silver line (4 μm in width).

References

Adapa, S., Gaur, V., Verma, N., *Chem. Eng. J.* **116**, 25 (2006).

Ajayan, P.M., Iijima, S., *Nature* **361**, 333 (1993).

Ang, K.H., Alexandrou, I., Mathur, N.D., Amaratunga, G.A., Haq, S., *Nanotechnology* **15**, 520 (2004).
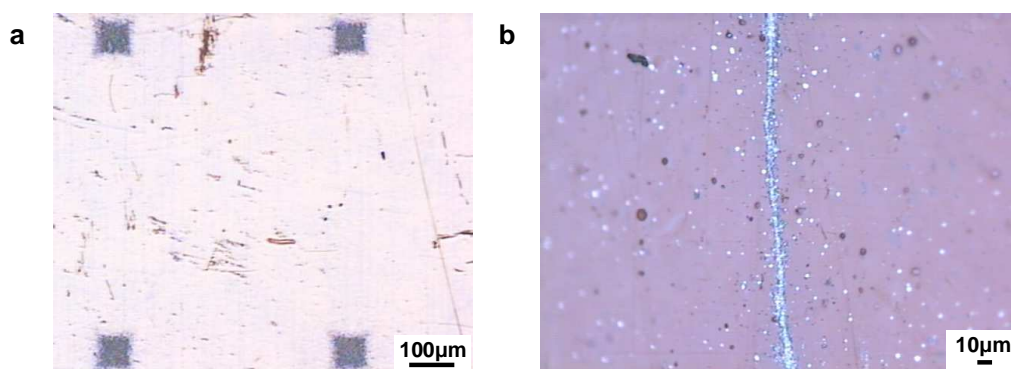
Ang, L.M., Andy Hor, T.S., Xu, G.Q., Tung, C.H., Zhao, S.P., Wang, J.L.S., *Carbon* **38**, 363 (2000).

Ang, L.M., Andy Hor, T.S., Xu, G.Q., Tung, C.H., Zhao, S., Wang, J.L.S., *Chem. Mat.* **11**, 2115 (1999).

Artamonov, M.F., Krasov, V.I., Paperny, V.L., *J. Phys. D* **34**, 3364 (2001).

Baker, R. T. K., *Carbon* **27**, 315 (1989).

Balazy, A., Podgórski, A., *J. Colloid Interface Sci.* **311**, 323 (2007).

Berkowitz, A.E., Walter, J.L., *J. Mater. Res.* **2**, 277 (1987).

Bird, R.T., Stewart, W.E., Lightfoot, E.N. Transport phenomena. New York, NY: Wiley (1960).

Borra, J.P., Goldman, A., Goldman, M., Boulaud, D., *J. Aerosol Sci.* **29**, 661 (1998).

Brayner, R., Ferrari-Iliou, R., Brivois, N., Djediat, S., Benedetti, M.F., Fiévet, F., *Nano Lett.* **6**, 866 (2006).

Brunauer, S., Emmett, P.H., Teller, E., *J. Am. Chem. Soc.* **60**, 309 (1938).

Busato, S., Belloli, A., Ermanni, P., *Sens. Actuator B* **123**, 840 (2007).

Byeon, J.H., Park, J.H., Yoon, K.Y., Hwang, J., *Small*, doi: 10.1002/smll.200700899 (2007).

Byeon, J.H., Park, J.H., Yoon, K.Y., Ko, B.J., Ji, J.H., Hwang, J., *Carbon* **44**, 2106 (2006).

Byeon, J.H., Yoon, H.S., Yoon, K.Y., Ryu, S.K., Hwang, J., *Surf. Coat. Technol.*, doi: 10.1016/j.surfcoat.2007.12.032 (2007b).

Byeon, J.H., Yoon, K.Y., Park, J.H., Hwang, J., *Carbon* **45**, 2313 (2007a).

Cádenas, G., Oliva, R., *Colloid Polym. Sci.* **281**, 27 (2003).

Cecchini, C., Verdenelli, M.C., Orpianesi, C., Dadea, G.M., Cresci, A., *J. Appl. Microbiol.* **97**, 371 (2004).

Charbonnier, M., Goepfert, Y., Romand, M., Leonard, D., *J. Adhes.* **80**, 1103 (2004).

Charbonnier, M., Romand, M., Goepfert, Y., Léonard, D., Bouadi, M., *Surf. Coat. Technol.* **200**, 5478 (2006).

Chen, C.-S., Chen, X.-H., Yang, Z., Li, W.-H., Xu, L.-S., Yi, B., *Diam. Relat. Mat.* **15**, 151 (2006).

Chen, D., Lu, Q., Zhao, Y., *Appl. Surf. Sci.* **253**, 1573 (2006).

Chen, M., Yu, H.-W., Chen, J.-H., Koo, H.-S., *Diam. Relat. Mat.* **16**, 1110 (2007).

Chen, S., Zeng, H., *Carbon* **41**, 1265 (2003).

Chen, W., Zhang, J., Cai, W., *Scr. Mater.* **48**, 1061 (2003).

Cheng, K., Yang, M.-H., Chiu, W.W.W., Huang, C.-Y., Chang, J., Ying, T.-F., Yang, Y., *Macromol. Rapid Commun.* **26**, 247 (2005).

Cho, J.S.H., Kang, H.-K., Wong, S.S., Shacham-Diamond, Y., *MRS Bull.* **18**, 31 (1993).

Cho, K.H., Park, J.E., Osaka, T., Park, S.G., *Electrochimi. Aata* **51**, 956 (2005).

Choi, H.C., Shim, M., Bangsaruntip, S., Dai, H., *J. Am. Chem. Soc.* **124**, 9058 (2002).

Das, D., Gaur, V., Verma, N., *Carbon* **42**, 2949 (2004).

Day, T.M. Unwin, P.R., Wilson, N.R., Macpherson, J.V., *J. Am. Chem. Soc.* **127**, 10639 (2005).

Deki, S., Akamatsu, K., Hatakenaka, Y., Mizuhata, M., Kajinami, A., *Nanostruct. Mater.* **11**, 59 (1999).

Devarajan, S., Bera, P., Sampath, S., *J. Colloid Interface Sci.* **290**, 117 (2005).

Ding, F., Rosén, A., Campbell, E.E.B., Falk, L.K.L., Bolton, K., *J. Phys. Chem. B* **110**, 7666 (2006).

Dravid, V.P., Host, J.J., Teng, M.H., Elliott, B., Hwang, J., Johnson, D.L., Mason, T.O., Weertman, J.R., *Nature* **374**, 602 (1995).

Dressick, W.J., Dulcey, C.S., Georger, Jr., J.H., Calvert, J.M., *Chem. Mater.* **5**, 148 (1993).

Ebbesen, T.W., Hiura, H., Bisher, M.E., Treacy, M.M.J., Shreeve-Keyer, J.L., Haushalter, R.C., *Adv. Mater.* **8**, 155 (1996).

Elliott, B.R., Host, J.J., Dravid, V.P., Teng, M.H., Hwang, J.-H., *J. Mater. Res.* **12**, 3328 (1997).

Esrom, H., *Appl. Surf. Sci.* **168**, 1 (2000).

Fan, L., Song, J., Hildebrand, P.D., Forney, C.F., *J. Appl. Microbiol.* **93**, 144 (2002).

Feng, Y., Yuan, H., *J. Mater. Sci.* **39**, 3241 (2004).

Flahaut, E., Agnoli, F., Sloan, J., O'Connor, C., Green, M.L.H., *Chem. Mat.* **14**, 2553 (2002).

Fu, P., Luan, Y., Dai, X., *J. Mol. Catal. A* **221**, 81 (2004).

Fukuhara, C., Kamata, Y., Igarashi, A., *Appl. Catal. A* **296**, 100 (2005).

Fullam, S., Cottell, D., Rensmo, H., Fitzmaurice, D., *Adv. Mater.* **12**, 1430 (2000).

Geissler, M., Bernard, A., Bietsch, A., Schmid, H., Michel, B., Delamarche, E., *J. Am. Chem. Soc.* **122**, 6303 (2000).

Gonzalez, D., Nasibulin, A.G., Baklanov, A.M., Shandakov, S.D., Brown, D.P., Queipo, P., Kauppinen, E.I., *Aerosol Sci. Technol.* **39**, 1064 (2005).

Gray, J.E., Norton, P.R., Griffiths, K., *Thin Solid Films* **484**, 196 (2005).

Griffiths, W.D., Bennett, A., Speight, S., Parks, S., *J. Hosp. Infect.* **61**, 242 (2005).

Guo, D.J., Li, H.L., *Carbon* **43**, 1259 (2005).

Guo, Z., Xie, Y., Hong, I., Kim, J., *Energy Conv. Manag.* **42**, 2005 (2001).

Hagberg, E.C., Scott, J.C., Shaw, J.A., von Werne, T.A., Maegerlein, J.A., Carter, K.R., *Small* **3**, 1703 (2007).

Harada, M., Toshima, N., Yoshida, K., Isoda, S., *J. Colloid Interface Sci.* **283**, 64 (2005).

Hasegawa, M., Yamachika, N., Shacham-Diamond, Y., Okinaka, Y., Osaka, R., *Appl. Phys. Lett.* **90**, 101916-1 (2007).

Hayashi, T., Hirono, S., Tomita, M., Umemura, S., *Nature* **381**, 772 (1996).

Helsper, C., Mölter, W., Löffler, F., Wadenpohl, C., Kaufmann, S., Wenninger, G., *Atmos. Environ.* **27A**, 1271 (1993).

Hendricks, T.R., Lee, I., *Thin Solid Films* **515**, 2347 (2006).

Hidber, P.C., Helbig, W., Kim, E., Whitesides, G.M., *Langmuir* **12**, 1375 (1996).

Holland, L., *Nature* **178**, 328 (1956).

Holstein, W. L., *J. Catal.* **152**, 42 (1995).

Horvath, H., Gangl, M., *J. Aerosol. Sci.* **34**, 1581 (2003).

Host, J.J., Block, J.A., Parvin, K., Dravid, V.P., Alpers, J.L., Sezen, T., LaDuca, R., *J. Appl. Phys.* **83**, 793 (1998).

Host, J.J., Dravid, V.P., Teng, M.H., *J. Mater. Res.* **13**, 2547 (1998a).

Host, J.J., Teng, M.H., Elliott, B.R., Hwang, J.-H., Mason, T.O., Johnson, D.L., Dravid, V.P., *J. Mater. Res.* **12**, 1268 (1997b).

Hozumi, A., Asakura, S., Fuwa, A., Shirahata, N., *J. Vac. Sci. Technol. A* **23**, 1029 (2005).

Huo, J., Song, H., Chen, X., Zhao, S., Xu, C., *Mater. Chem. Phys.* **101**, 221 (2007).

Hwang, J.-H., Draid, V.P., Teng, M.H., Host, J.J., Elliott, B.R., Johnson, D.L., Mason, T.O., *J. Mater. Res.* **12**, 1076 (1997).

Illán-Gómez, M.J., Linares-Solano, A., Radovic, L.R., Salinas-Martínez de Lecea, C., *Energy Fuels* **10**, 158 (1996).

Jeon, H.J., Yi, S.C., Oh, S.G., *Biomaterials* **24**, 4921 (2003).

Jiang, J., Lee, M.-H., Biswas, P., *J. Electrost.* **65**, 209 (2007).

Jiang, L., Gao, L., *Carbon* **41**, 2923 (2003).

Jiao, J., Seraphin, S., *J. Appl. Phy.* **83**, 2442 (1998).

Jiao, J., Seraphin, S., *J. Phys. Chem. Solids* **61**, 1055 (2000).

Kalberer, M., Ammann, M., Gaggeler, H.W., Baltensperger, U., *Atmos. Environ.* **33**, 2815 (1999).

Kamm, S., Möhler, O., Naumann, K.H., Saathoff, H., Schurath, U., *Atmos. Environ.* **33**, 4651 (1999).

Karski, S., Witońska, I., Rogowski, J., Gołuchowska, J., *J. Mol. Catal. A* **240**, 155 (2005).

Khoperia, T.N., Tabatadze, T.J., Zedgenidze, T.I., *Electrochim. Acta* **42**, 3049 (1997).

Kim, B., Sigmund, W.M., *Langmuir* **20**, 8239 (2004).

Kim, J.-T., Chang, J.-S., *J. Electrost.* **63**, 911 (2005).

Kordás, K., Békési, J., Bali, K., Vajtai, R., Nánai, L., George, T.F., Leppävuori, S., *J. Mater. Res.* **14**, 3690 (1999).

Krasik, Y.E., Gleizer, S., Chirko, K., Gleizer, J.Z., Felsteiner, J., Bernshtam, V., Matacotta, F.C., *J. Appl. Phys.* **99**, 063303-1 (2006).

Kreitz, S., Penache, C., Thomas, M., Klages, C.P., *Surf. Coat. Technol.* **200**, 676 (2005).

Kuznetsov, B.V., Rakhmanova, T.A., Popovicheva, O.B., Shonija, N.K., *J. Aerosol. Sci.* **34**, 1465 (2003).

Lambert, S., Ferauche, F., Heinrichs, B., Tcherkassova, N., Pirard, J., Alié, C., *J. Non-Cryst. Solids* **352**, 2751 (2006).

Lee, I., Hammond, P.T., Rubner, M.F., *Chem. Mater.* **15**, 4583 (2003).

Lee, Y.W., Choi, D.K., Park, J.W., *Carbon* **40**, 1409 (2002).

Li, C.Y., Wan, Y.Z., Wang, J., Wang, Y.L., Jiang, X.Q., Han, L.M., *Carbon* **36**, 61 (1998).

Lin, J.-S., Tsai, C.-J., *J. Aerosol Sci.* **34**, 569 (2003).

Lin, W.H., Hwang, C.Y., Chang, H.F., *Appl. Catal. A* **162**, 71 (1997).

Little, R.B., *J. Clust. Sci.* **14**, 135 (2003).

Liu, H., Mao, G., Meng, S., *J. Mol. Catal.* **74**, 275 (1992).

Lok, C.N., Ho, C.M., Chen, R., He, Q.Y., Yu, W.Y., Sun, H., Tam, P.K.H., Chiu, J.F., Che, C.M., *J. Proteome Res.* **5**, 916 (2006).

Lu, A.H., Li, W.C., Matoussevitch, N., Spliethoff, B., Bonnemann, H., Schuth, F., *Chem. Commun.*, 98 (2005).

Lu, S.-Y., Lin, Y.-Z., *Thin Solid Films* **376**, 67 (2000).

Lu, Y., Zhu, Z., Liu, Z., *Carbon* **43**, 369 (2005).

Matatov-Meytal, Y., Sheintuch, M., *Appl. Catal. A* **231**, 1 (2002).

Mochida, I., Kawano, S., Shirahama, N., Enjoji, T., Moon, S.H., Sakanishi, K.S., Korai, Y., Yasutake, A., Yoshikawa, M., *Fuel* **80**, 2227 (2001).

Ma, X., Li, X., Lun, N., Wen, S., *Mater. Chem. Phys.* **97**, 351 (2006).

Main, C.E., *Environ. Int.* **29**, 347 (2003).

Maricq, M.M., *Combust. Flame* **141**, 406 (2005).

Marquez-Alvarez, C., Rodriguez-Ramos, I., Guerrero-Ruiz, A., *Carbon* **34**, 339 (1996).

Marusina, V.I., Filimonenko, V.N., *Powder Metall. Met. Ceram.* **23**, 432 (1984).

Matsumoto, T., Komatsu, T., Arai, K., Yamazaki, T., Kijima, M., Shimizu, H., Takasawa, Y., Nakamura, J., *Chem. Commun.* **7**, 840 (2004).

Maus, R., Goppelsröder, A., Umhauer, H., *Atmos. Environ.* **35**, 105 (2001).

Melaiye, A., Sun, Z., Hindi, K., Milsted, A., Ely, D., Reneker, D.H., Tessier, C.A., Youngs, W.A., *J. Am. Chem. Soc.* **127**, 2285 (2005).

Messerer, A., Niessner, R., Pöschl, U., *J. Aerosol Sci.* **34**, 1009 (2003).

Metz, K.M., Divya, D., Hamers, R.J., *J. Phys. Chem. C* **111**, 7260 (2007).

Mizsei, J., Sipilä, Lantto, V., *Sens. Actuator B* **47**, 139 (1998).

Mochida, I., Korai, Y., Shirahama, M., Kawano, S., Hada, T., Seo, Y., Yoshikawa, M., Yasutake, A., *Carbon* **38**, 227 (2000).

Moon, J.S., Park, K.K., Kim, J.H., Seo, G., *Appl. Catal. A* **201**, 81 (2000).

Morrison, M.L., Buchanan, R.A., Liaw, P.K., Berry, C.J., Brigmon, R.L., Riester, L., Abernathy, H., Jin, C., Narayan, R.J., *Diam. Relat. Mater.* **15**, 138 (2006).

Neogrády, P., Kellö, V., Urban, M., Sadlej, A.J., *J. Chem Sci.* **117**, 311 (1997).

Norkus, E., Vaškelis, A., Jačiauskienė, J., Stalnionienė, I., Stalnionis, G., *Electrochim. Acta* **51**, 3495 (2006).

Oleshko, V.P., *J. Mol. Catal. A* **249**, 4 (2006).

Papo, N., Shai, Y., *J. Biol. Chem.* **280**, 10378 (2005).

Park, B.J., Park, S.J., Ryu, S.K., *J. Colloid Interf. Sci.* **217**, 142 (1999).

Park, S.H., Kim, C., Jeong, Y.I., Lim, D.Y., Lee, Y.E., Yang, K.S., *Synth. Met.* **146**, 207 (2004).

Park, S.J., Jang, Y.S., *J. Colloid Interface Sci.* **261**, 238 (2003).

Park, S.J., Jang, Y.S., Shim, J.W., Ryu, S.K., *J. Colloid Interface Sci.* **260**, 259 (2003).

Park, S.J., Kim, B.J., *J. Colloid Interface Sci.* **282**, 124 (2005a).

Park, S.J., Kim, B.J., *J. Colloid Interface Sci.* **292**, 493 (2005b).

Patel, K., Kapoor, S., Dave, D.P., Mukherjee, T., *Int. J. Quantum Chem.* **63**, 557 (2005).

Persson, K., Jansson, K., Järås, S.G., *J. Catal.* **245**, 401 (2007).

Planeix, J.M., Coustel, N., Coq, B., Brotons, V., Kumbhar, P.S., Dutartre, R., Geneste, P., Bernier, P., Ajayan, P.M., *J. Am. Chem. Soc.* **116**, 7935 (1994).

Porter, L.A., Choi, H.C., Ribbe, A.E., Buriak, M., *Nano Lett.* **2**, 1067 (2002).

Pradhan, B.K., Toba, T., Kyotani, T., Tomita, A., *Chem. Mater.* **10**, 2510 (1998).

Prissanaroon, W., Brack, N., Pigram, P.J., Hale, P., Kappen, P., Liesegang, J., *Thin Solid Films* **477**, 131 (2005).

Qu, L., Dai, L., *J. Am. Chem. Soc.* **127**, 10806 (2005).

Qu, L., Dai, L., Osawa, E., *J. Am. Chem. Soc.* **128**, 5523 (2006).

Rodriguez, N.M., *J. Mater. Res.* **8**, 3233 (1993).

Sano, N., Wang, H., Alexandrou, I., Chhowalla, M., Teo, K.B.K., Limura, K., *J. Appl. Phy.* **92**, 2783 (2002).

Saito, Y., *Carbon* **33**, 979 (1995).

Saito, Y., Yoshikawa, T., Okuda, M., Fujimoto, N., *Chem. Phys. Lett.* **212**, 379 (1993a).

Saito, Y., Yoshikawa, T., Okuda, M., Fujimoto, N., Sumiyama, K., Suzuki, K., Kasuya, A., Nishina, Y., *J. Phys. Chem. Solids* **54**, 1849 (1993b).

Saito, Y., Yoshikawa, T., Okuda, M., Fujimoto, N., Yamamuro, S., Wakoh, K., Sumiyama, K., Suzuki, K., Kasuya, A., Nishina, Y., *J. Appl. Phys.* **75**, 134 (1994).

Satishkumar, B.C., Vogl, E.M., Govindaraj, A., Rao, C.N.R., *J. Phys. D* **29**, 3173 (1996).

Schaefers, S., Rast, L., Stanishevsky, A., *Mater. Lett.* **60**, 706 (2006).

Schwyn, S., Garwin, E., Schmidt-Ott, A., *J. Aerosol. Sci.* **19**, 639 (1988).

Schrott, A.G., Braren, B., O'Sullivan, E.J.M., Saraf, R.F., Bailey, P., Roldan, J., *J. Electrochem. Soc.* **142**, 944 (1995).

Seo, W.S., Lee, J.H., Sun, X., Suzuki, Y., Mann, D., Liu, Z., Terashima, M., Yang, P.C., Mcconnell, M.W., Nishimura, D.G., Dai, H., *Nat. Mater.* **5**, 971 (2006).

Seraphin, S., Zhou, D., Jiao, J., *J. Appl. Phy.* **80**, 2097 (1996).

Sergiienko, R., Shibata, E., Akase, Z., Suwa, H., Shindo, D., Nakamura, T., *J. Mater. Res.* **21**, 2524 (2006).

Setlur, A.A., Dai, J.Y., Lauerhaas, J.M., Washington, P.L., Chang, R.P.H., *J. Mater. Res.* **13**, 2139 (1998).

Shah, P., Kevrekidis, Y., Benziger, J., *Langmuir* **15**, 1584 (1999).

Shen, W., Guo, Q., Zhang, Y., Liu, Y., Zheng, J., Cheng, J., Fan, J., *Colloid Surf. A* **273**, 147 (2006).

Shirahama, N., Mochida, I., Korai, Y., Choi, K.H., Enjoji, T., Shimohara, T., Yasutake, A., *Appl. Catal. B* **52**, 173 (2004).

Shirahama, N., Moon, S.H., Choi, K.H., Enjoji, T., Kawano, S., Korai, Y., Tanoura, M., Mochida, I., *Carbon* **40**, 2605 (2002).

Simonin, L., Lafont, U., Tabrizi, U., Schmidt-Ott, A., Kelder, E.M., *J. Power Sources*, doi:10.1016/j.jpowsour.2007.06.197 (2007).

Šimor, M., Ráhel, J., Černák, M., Imahori, Y., Štefečka, M., Kando, M., *Surf. Coat. Technol.* **172**, 1 (2003).

Smith, J.M. Chemical engineering kinetics. New York, NY: McGraw-Hill (1996).

Sondi, I., Salopek-Sondi, B., *J. Colloid Interface Sci.* **275**, 177 (2004).

Stoimenov, P.K., Klinger, R.L., Marchin, G.L., Klabunde, K.J., *Langmuir* **18**, 6679 (2002).

Sugimura, H., Hanji, T., Takai, O., Masuda, T., Misawa, H., *Electrochim. Acta* **47**, 103 (2001).

Sun, Y.Y., Xu, H., Feng, Y.P., Huan, A.C.H., Wee, A.T.S. *Surf. Sci.* **548**, 309 (2004).

Tai, C.-C., Su, F.-Y., Sun, I.-W., *Electrochim. Acta* **50**, 5504 (2005).

Tamai, H., Katsu, N., Ono, K., Yasuda, H., *Carbon* **39**, 1963 (2001).

Teng, M.-H., Tsai, S.-W., Hsiao, C.-I., Chen, Y. -D., *J. Alloy. Compd.* **434-435**, 678 (2007).

Terrones, M., *Int. Mater. Rev.* **49**, 325 (2004).

Thomas, D., Penicot, P., Contal, P., Leclerc, D., Vendel, J., *Chem. Eng. Sci.* **56**, 3549 (2001).

Tian, Z.Q., Jiang, S.P., Liang, Y.M., Shen, P.K., *J. Phy. Chem. B* **110**, 5343 (2006).

Tomita, S., Hikita, M., Fujii, M., Hayashi, S., Yamamoto, K., *Chem. Phys. Lett.* **316**, 361 (2000).

Toshima, N., Harada, M., Yamazaki, Y., Asakura, K., *J. Phys. Chem.* **96**, 9927 (1992).

Toshima, N., Harada, M., Yonezawa, T., Kushihashi, K., Asakura, K., *J. Phys. Chem.* **95**, 7448 (1991).

Toshima, N., Kushihashi, K., Yonezawa, T., Hirai, H., *Chem. Lett.*, 1769 (1989).

Touchais-Papet, E., Charbonnier, M., Romand, M., *Appl. Surf. Sci.* **138-139**, 557 (1999).

Tsai, C.-J., Lin, J.-S., Aggarwal, S.G., Chen, D.-R., *Aerosol Sci. Technol.* **38**, 131 (2004).

Tsai, C.-J., Lu, H.-C., *Aerosol Sci. Technol.* **22**, 172 (1995).

Tsai, W.T., Chang, C.Y., Ho, C.Y., Chen, L.Y., *Sep. Sci. Technol.* **35**, 1635 (2000).

Ugarte, D., Châtelain, W., de Heer, W.A., *Science* **274**, 1897 (1996).

Ugarte, D., Stöckli, T., Bonard, J.M., Châtelain, W., de Heer, W.A., *Appl. Phys. A* **67**, 101 (1998).

Vargo, T.G., Gardella, Jr., J.A., Calvert, J.M., Chen, M.-S., *Science* **262**, 1711 (1993).

Verdenelli, M.C., Cecchini, C., Orpianesi, C., Dadea, G.M., Cresci, A., *J. Appl. Microbiol.* **94**, 9 (2003).

Vilaplana-Ortego, E., Alcañiz-Monge, J., Cazorla-Amorós, D., Linares-Solano, A., *Fuel Process. Technol.* **77-78**, 445 (2002).

Walker, C.M., Ko, G., *Environ. Sci. Technol.* **41**, 5460 (2007).

Wang, C.-C., Chen, D.-H., Huang, T.-C., *Colloid Surf. A* **189**, 145 (2001).

Wang, F., Arai, S., Endo, M., *Electrochem. Commun.* **6**, 1042 (2004).

Wang, J.M., Wen, L.X., Wang, Z.H., Chen, J.F., *Mater. Chem. Phys.* **96**, 90 (2006).

Wang, J.N., Zhang, L., Yu, F., Sheng, Z.M., *J. Phys. Chem. B* **111**, 2119 (2007).

Wang, K.-W., Chung, S.-R., Perng, T.P., *J. Alloy. Compd.* **417**, 60 (2006).

Wang, Z.H., Choi, C.J., Kim, B.K., Kim, J.C., Zhang, Z.D., *Carbon* **41**, 1751 (2003).

Watters, Jr., R.L., DeVoe, J.R., Shen, F.H., Small, J.A., Marinenko, R.B., *Anal. Chem.* **61**, 1826 (1989).

Weber, A.P., Seipenbusch, M., Kasper, G., *J. Phys. Chem. A* **105**, 8958 (2001).

Weller, R.A., Ryle, W.T., Newton, A.T., McMahon, M.D., Miller, T.M., Magruder, III, R.H., *IEEE Trans. Nanotehcnol.* **2**, 154 (2003).

Wildgoose, G.G., Banks, C.E., Compton, R.G., *Small* **2**, 182 (2006).

Xiaomin, W., Bingshe, X., Husheng, J., Xuguang, L., Hideki, I., *J. Phys. Chem. Solids* **67**, 871 (2006).

Xing, Y., *J. Phys. Chem. B* **108**, 19255 (2004).

Xu, C., Chen, J., Cui, Y., Han, Q., Choo, H., Liaw, P.K., Wu, D., *Adv. Eng. Mater.* **8**, 73 (2006).

Xu, C., Wu, G., Liu, Z., Wu, D., Meek, T.T., Han, Q., *Mater. Res. Bull.* **39**, 1499 (2004).

Xu, D., Kang, E.T., Neoh, K.G., Zhang, Y., Tay, A.A.O., Ang, S.S., Lo, M.C.Y., Vaidyanathan, K., *J. Phys. Chem. B* **106**, 12508 (2002).

Xu, L., Liao, J., Huang, L., Ou, D., Guo, Z., Zhang, H., Ge, C., Gu, N., Liu, J., *Thin Solid Films* **434**, 121 (2003).

Xu, Q., Zhang, L., Zhu, J., *J. Phys. Chem. B* **107**, 8294 (2003).

Yanagimoto, H., Deki, S., Akamatsu, K., Gotoh, K., *Thin Solid Films* **491**, 18 (2005).

Yang, C.-C., Wan, C.-C., Wang, Y.-Y., *J. Colloid Interface Sci.* **279**, 433 (2004).

Yang, C.M., Kaneko, K., *J. Colloid Interface Sci.* **246**, 34 (2002).

Yang, R.T. Gas separation by adsorption process. UK: Imperial College Press (1997).

Ye, X.R., Lin, Y., Wai, C.M., *Chem. Commun.* **5**, 642 (2003).

Yoon, K.Y., Byeon, J.H., Park, J.H., Hwang, J., *Sci. Total Environ.* **373**, 572 (2007).

Yu, R., Chen, L., Liu, Q., Lin, J., Tan, K.-L., Ng, S.C., Chan, H.S.O., Xu, G.-Q., Andy Hor, T.S., *Chem. Mater.* **10**, 718 (1998).

Zawadzki, J., Wiśniewski, M., *Carbon* **40**, 119 (2002).

Zhang, J.Y., Boyd, I.W., *Appl. Phys. A*, **65**, 379 (1997).

Zhang, J.-Y., Boyd, I.W., *Thin Solid Films* **318**, 234 (1998).

Zhang, J.-Y., King, S.L., Boyd, I.W., Fang, Q., *Appl. Surf. Sci.* **109**, 487 (1997).

Zhang, S., Fu, R., Wu, D., Xu, W., Ye, Q., Chen, Z., *Carbon* **42**, 3209 (2004).

Zhao, X., Hirogaki, K., Tabata, I., Okubayashi, S., Hori, T., *Surf. Coat. Technol.* **201**, 628 (2006).

Zheng, F., *Adv. Colloid Interface Sci.* **97**, 255 (2002).

Abstract in Korean

본 논문에서는 무전해도금, 스파크생성 및 무전해도금과 스파크생성 기술을 통합한 입자 생성기술을 통해 나노입자를 생성하고 물리화학적 특성을 평가하였다. 무전해도금으로는 활성탄소섬유와 탄소나노튜브 표면에 구리와 은 나노입자를 생성하였고, 스파크생성으로는 단성분 및 이성분 금속 에어로졸 나노입자, 탄소 및 탄소-금속 캡슐 에어로졸 입자를 생성하였다. 무전해도금과 스파크생성 통합에서는 스파크생성 금속나노입자를 무전해도금 개시촉매로 활용하여 활성탄소섬유 위의 은 코팅과 폴리이미드 필름 위의 은 및 구리 마이크로패터닝 수행하였다.

키워드: 나노입자생성; 무전해도금; 스파크생성